

Mesh-free RBF-based discretizations for hydrodynamic stability analysis

Tianyi Chu* and Oliver T. Schmidt[†]
Department of Mechanical and Aerospace Engineering, Jacobs School of Engineering, UCSD, 9500 Gilman Drive, La
Jolla, CA 92093-0411, USA

Radial basis function-based finite differences (RBF-FD) are used to develop a high-order mesh-free hydrodynamic stability analysis tool for complex geometries. Polyharmonic spline RBFs with polynomial augmentation (PHS+poly) are used to construct the discrete linearized Navier-Stokes and resolvent operators on arbitrarily scattered nodes. The PHS+poly discretization is shown to yield accurate, stable, and computationally efficient discretizations of the large hydrodynamic stability matrix problems arising in two-dimensional classical linear theory and resolvent analysis. The mean-flow stability of the wake behind a cylinder in the vicinity of the critical point is studied using both theories. The predicted flow instabilities, including the vortex shedding frequency and associated coherent structures, closely match those reported in the literature.

I. Nomenclature

linearized Navier-Stokes operator around the mean-flow and its discretization $\mathcal{L}_{\overline{u}}, L_{\overline{u}}$ RBF-based interpolation matrix D global RBF-based differentiation matrix Δr local characteristic distance of the grid = magnitude of fluctuation ϵ input/forcing vector, local and global f RBF interpolation coefficients γ L linear operator λ stability eigenvalue exponent of the polyharmonic spline m local stencil size nN total amount of nodes ∇ the gradient pressure \mathcal{P} . \boldsymbol{P} prolongation operator and its discretization P(x)multivariate polynomial degree of the polynomial augmentation $\phi(r)$ radial function \mathcal{R}, R resolvent operator and its discretization = Re Reynolds number resolvent singular value σ St Strouhal number u, vhorizontal and vertical velocity components velocity vector, local and global u local RBF weights weight matrices angular frequency node location x

^{*}Graduate Student, Department of Mechanical and Aerospace Engineering.

[†]Assistant Professor, Department of Mechanical and Aerospace Engineering, Senior Member AIAA.

Superscripts

 $(\cdot)'$ = fluctuating component

 (\cdot) = normal mode

 $\overline{(\cdot)}$ = mean component

 (\cdot) = frequency-domain representation

II. Introduction

Flow instabilities and large-scale coherent structures are ubiquitous in fluid mechanics. In the last century, classical linear stability analysis has been applied to investigate the growth of small disturbances for laminar flows. Examples include cylinder wakes [1] [2], non-parallel shear flows [3], and thin aerofoil wakes [4]. However, linear stability analysis around steady laminar base flow often fails to predict finite-amplitude flow instabilities arising from nonlinear interactions. Despite violating the basic assumptions of linear theory, the use of mean-flows for linear analysis has been successful at predicting coherent flow features in a variety of flows, including cylinder wakes [5], open cavity flows [7], and turbulent or transitional jets [8] [9]. More general applications to broadband turbulent flows are still wanting. More recently, resolvent, or input-output analysis, has revealed its potential to predict large-scale coherent structures in turbulent flows accurately. The resolvent operator is obtained from the forced linearized system and forms a transfer function between forcings and responses. Within the laminar regime, resolvent analysis has been used to examine the linear response to external body forces and perturbations for channel flow [10, 11], boundary layers [12, 13], and jets [14-16]. Unlike classical linear stability analysis, the input-output perspective also provides a mathematically rigorous framework for analyzing turbulent mean-flows by identifying the forcing with the Reynolds stresses in the perturbation-interaction terms in the Reynolds-decomposed Navier-Stokes equations [17] [18]. The applicability of linear stability analysis on turbulent mean-flows with strong convective instabilities has been demonstrated by Beneddine et al. [19]. Applications of resolvent analysis to identify large-scale coherent motion based on turbulent mean-flows include near-wall flows [17, 18], boundary layers [20, 21], incompressible [14] or compressible jets [15, 22, 23], and flows over an airfoil [24]. Both classical linear stability and resolvent analysis require, in their most basic form, the construction large matrices that have to be decomposed into their singular- or eigen-components. This work proposes an approach based on radial basis functions (RBFs) to construct the large, sparse operators that are at the core of hydrodynamic stability analysis.

The key novelty of this work is the development of a high-order mesh-free framework for hydrodynamic stability analysis based on RBF-FD discretization. The RBF methodology originated from the idea of scattered data interpolation by Hardy [25] and provided a systematic way to approximate multivariate functions on arbitrarily scattered nodes. RBF-based methods facilitate maximum flexibility in meshing complex geometries, local grid refinement, and local adjustments to the order of accuracy of the discretization. The idea of incorporating RBFs and the classical finite difference (FD) method was first proposed in a conference presentation by Tolstykh [26]. The so-called RBF-FD method generalizes the classical FD methods to arbitrary node layouts by approximating the desired function based on RBFs. Common choices for RBFs include Gaussian (GA), multiquadrics (MQ), and inverse multiquadrics (IMQ). Refer to [27] for a detailed overview. These RBF types have the shape parameter as a free parameter, which in turn significantly impacts both accuracy and stability. Recently, RBF-FD approximations based on polyharmonic splines (PHS) that are augmented with polynomials (PHS+poly), that were first introduced in Flyer et al. [28], and that do not require a shape parameter, have revealed their potential to achieve high-order accuracy. In particular, Flyer et al. [29] showed that local PHS+poly generated RBF-FD stencils provide high-order accuracy for derivative approximations and eliminate the stagnation errors under node refinement. Bayona et al. [30] used PHS+poly for solving elliptic PDEs and relied on a larger stencil size near domain boundaries to avoid the Runge phenomenon. The feasibility of this strategy was later analytically confirmed by Bayona [31] using RBFs in a closed-form. Numerical demonstrations for 2-D and 3-D examples were presented in Bayona et al. [32]. Several comparisons have been made to other higher-order mesh-free methods, including polynomial least-squares approximations [29], the RBF-GA method near the flat limit [33], and the moving least-squares (MLS) method [34]. All studies conclude that PHS+poly-based RBF-FDs perform well in terms of accuracy, robustness, and computational efficiency.

As a test case for the proposed mesh-free framework, we study the 2-D cylinder wake. It is well-known that the cylinder wake becomes unstable beyond the critical Reynolds number $Re_c \simeq 47$ due to a Hopf bifurcation, which leads

to the periodic von Kármán vortex shedding, see e.g. [35, 36]. Linear stability analysis around the mean-flow accurately identifies the vortex shedding frequency [2, 37, 38] and the unsteady flow structures [5, 6]. Symon et al. [39] futher demonstrated that the leading linear stability and resolvent modes for the cylinder wake are nearly identical. We here conduct both global stability as well resolvent analyses of the cylinder wake mean-flow within the 2-D laminar regime, $47 \lesssim \text{Re} \lesssim 188$ (beyond which the flow becomes three-dimensional [40, 41]).

III. Hydrodynamic stability analysis for incompressible flows

The motion of a general incompressible Newtonian fluid is governed by the Navier-Stokes equations,

$$\frac{\partial \mathbf{u}}{\partial t} + (\mathbf{u} \cdot \nabla) \mathbf{u} = -\nabla p + \text{Re}^{-1} \nabla^2 \mathbf{u}, \tag{1a}$$

$$\nabla \cdot \boldsymbol{u} = 0. \tag{1b}$$

All variables are nondimensionalized by the velocity scale U_{∞} and the length scale L, and Re denotes the Reynolds number. We take the Reynolds decomposition of the, here two-dimensional, flow velocity, $\mathbf{u} = [u, v]^T$, and pressure, p, fields into the mean and small fluctuating components, $\overline{(\cdot)}$ and $(\cdot)'$, respectively, as

$$u = \overline{u} + \epsilon u', \quad p = \overline{p} + \epsilon p'.$$
 (2)

A small parameter ϵ represents the magnitude of the fluctuating quantities. The resulting governing equations for the fluctuations are

$$\frac{\partial \mathbf{u}'}{\partial t} + (\overline{\mathbf{u}} \cdot \nabla) \mathbf{u}' + (\mathbf{u}' \cdot \nabla) \overline{\mathbf{u}} = -\nabla p' + \operatorname{Re}^{-1} \nabla^2 \mathbf{u}' + f', \tag{3a}$$

$$\nabla \cdot \boldsymbol{u}' = 0, \tag{3b}$$

where we combined the two terms involving products of fluctuating quantities into a single term,

$$f' = \epsilon \left[-(u' \cdot \nabla) u' + \overline{(u' \cdot \nabla) u'} \right], \tag{4}$$

which we later either neglect or model.

Classical (temporal) linear stability analysis investigates fluctuations with complex frequency $\lambda = \lambda_r + i\lambda_i$, where λ_r is the exponential growth rate and λ_i the oscillation frequency. The fluctuations are assumed to be infinitesimally small with $\epsilon \ll 1$, see e.g., Schmid and Henningson [42]. The forcing term, f', is therefore negligible at O(1). Substituting perturbations of the form $[u', p'](x, t) = [\tilde{u}, \tilde{p}](x)e^{\lambda t}$ into the governing equations (3) yields the linear stability equations,

$$\lambda \tilde{\boldsymbol{u}} + (\overline{\boldsymbol{u}} \cdot \nabla) \, \tilde{\boldsymbol{u}} + (\tilde{\boldsymbol{u}} \cdot \nabla) \, \overline{\boldsymbol{u}} = -\nabla p + \operatorname{Re}^{-1} \nabla^2 \tilde{\boldsymbol{u}}, \tag{5a}$$

$$\nabla \cdot \tilde{\boldsymbol{u}} = 0. \tag{5b}$$

The above equations can be written in a compact operator notation as

$$\lambda \mathcal{P} \mathcal{P}^T \begin{pmatrix} \tilde{u} \\ \tilde{p} \end{pmatrix} = \mathcal{L}_{\overline{u}} \begin{pmatrix} \tilde{u} \\ \tilde{p} \end{pmatrix}, \tag{6}$$

where

$$\mathcal{L}_{\overline{u}} \equiv \begin{pmatrix} -(\overline{u} \cdot \nabla) () - [() \cdot \nabla] \overline{u} + Re^{-1} \nabla^2 & -\nabla \\ \nabla \cdot () & 0 \end{pmatrix}$$
 (7)

is the linearized Navier-Stokes (LNS) operator around the mean-flow, \mathcal{P} is the prolongation operator that extends the velocity vector $[u, v]^T$ into $[u, v, 0]^T$, and its transpose is the restriction operator that extracts the velocity vector from the extended state vector. Equation (6) is a generalized eigenvalue problem, and the eigenvector associated with the eigenvalue with the largest real part ought to predict the dominant instability mechanism of the flow.

For more general cases of finite amplitude fluctuations, the nonlinear interactions in equation (4) are no longer negligible, and we may consider the more general equation 3. Within the resolvent framework of turbulent flows, we

interpret the nonlinear interaction terms in f' as external forcing to the otherwise linear dynamics. This interpretation was first proposed by McKeon and Sharma [17].

By assuming a normal mode form for the fluctuating components, $[u', p', f'](x,t) = [\hat{u}, \hat{p}, \hat{f}](x)e^{i\omega t} + c.c.$, where ω is the angular frequency, or equivalently by taking the Fourier transform, we obtain the frequency-domain representation of the governing equations (3a) and (3b),

$$i\omega\hat{\boldsymbol{u}} + (\overline{\boldsymbol{u}}\cdot\nabla)\,\hat{\boldsymbol{u}} + (\hat{\boldsymbol{u}}\cdot\nabla)\,\overline{\boldsymbol{u}} = -\nabla\hat{\boldsymbol{p}} + \mathrm{Re}^{-1}\nabla^2\hat{\boldsymbol{u}} + \hat{\boldsymbol{f}},\tag{8a}$$

$$\nabla \cdot \hat{\boldsymbol{u}} = 0. \tag{8b}$$

Following the approach by Sipp and Marquet [13], we write equations (8) in a compact form as

$$\hat{\boldsymbol{u}} = \mathcal{R}(\omega)\hat{\boldsymbol{f}},\tag{9}$$

where $\mathcal{R}(\omega) = \mathcal{P}^T \left(i\omega\mathcal{P}\mathcal{P}^T - \mathcal{L}_{\overline{u}}\right)^{-1}\mathcal{P}$ is the resolvent operator. Equation (9) linearly relates the input, or forcing, \hat{f} , to the output, or response, \hat{u} . Input-output, or resolvent analysis, seeks pairs of optimal forcings and corresponding responses that maximize the gain, σ^2 , defined as the ratio of the energy of the response to the energy of the forcing,

$$\sigma^{2}(\hat{f};\omega) = \frac{\|\hat{\boldsymbol{u}}\|_{u}^{2}}{\|\hat{f}\|_{f}^{2}} = \frac{\left\langle \mathcal{R}(\omega)\hat{f}, \mathcal{R}(\omega)\hat{f} \right\rangle_{u}}{\left\langle \hat{f}, \hat{f} \right\rangle_{f}}.$$
(10)

The energy of the response and the forcing are measured in the norms $\|\cdot\|_u$ and $\|\cdot\|_f$, induced by the inner products

$$\langle \hat{\boldsymbol{u}}_1, \hat{\boldsymbol{u}}_2 \rangle_u = \int_{\Omega} \hat{\boldsymbol{u}}_2^*(\boldsymbol{x}, \omega) W_u(\boldsymbol{x}) \hat{\boldsymbol{u}}_1(\boldsymbol{x}, \omega) \, \mathrm{d}\boldsymbol{x} \qquad \text{and} \qquad \left\langle \hat{\boldsymbol{f}}_1, \hat{\boldsymbol{f}}_2 \right\rangle_f = \int_{\Omega} \hat{\boldsymbol{f}}_2^*(\boldsymbol{x}, \omega) W_f(\boldsymbol{x}) \hat{\boldsymbol{f}}_1(\boldsymbol{x}, \omega) \, \mathrm{d}\boldsymbol{x}$$
(11)

on the output and input spaces, respectively. W_u and W_f are two Hermitian matrices that contain variable weights that define the energy. Equation ($\overline{10}$) is solved by the Schmidt decomposition to the resolvent operator

$$\mathcal{R}(\omega) = \sum_{j=1}^{\infty} \sigma_j(\omega) \hat{\boldsymbol{u}}_j(\boldsymbol{x}, \omega) \otimes \hat{\boldsymbol{f}}_j(\boldsymbol{x}, \omega)$$
(12)

in terms of the inner products (II), where \otimes denotes the Kronecker product. In practice, that is for discrete data, it is solved by the singular value decomposition. The output modes, $\hat{\boldsymbol{u}}_j$, and input modes, $\hat{\boldsymbol{f}}_j$, are orthogonal in their respective inner products, that is, $\langle \hat{\boldsymbol{u}}_j, \hat{\boldsymbol{u}}_k \rangle_u = \langle \hat{\boldsymbol{f}}_j, \hat{\boldsymbol{f}}_k \rangle_f = \delta_{jk}$. The modes are ordered by the associated singular value, σ_j . It can be verified that the input and output modes are related through

$$\mathcal{R}(\omega)\hat{\boldsymbol{f}}_{j} = \sigma_{j}(\omega)\hat{\boldsymbol{u}}_{j}, \tag{13}$$

which provides a physical interpretation of the singular values and vectors.

The remainder of this paper is dedicated to constructing the discrete LNS, $L_{\overline{u}}$, and resolvent, $R(\omega)$, operators using PHS+poly RBF-FD.

IV. Radial basis functions (RBFs)

The method of radial basis functions (RBFs) approximates a given function g(x) using a set of smooth radial functions $\phi(r)$. RBF discretizations seek the interpolant

$$s(x) = \sum_{j=1}^{n} \gamma_j \phi(\|x - x_j\|)$$
 (14)

such that $s(x_j) = g(x_j)$ for $j = 1, 2, \dots, n$, where $\{x_j\}_{j=1}^n$ is a set of scattered nodes, and $\|\cdot\|$ denotes the standard Euclidean norm. The interpolation coefficients $\gamma_1, \dots, \gamma_n$ are found by solving the linear system

$$\begin{bmatrix}
\phi(\|x_{1}-x_{1}\|) & \phi(\|x_{1}-x_{2}\|) & \cdots & \phi(\|x_{1}-x_{n}\|) \\
\phi(\|x_{2}-x_{1}\|) & \phi(\|x_{2}-x_{2}\|) & \cdots & \phi(\|x_{2}-x_{n}\|) \\
\vdots & \vdots & & \vdots \\
\phi(\|x_{n}-x_{1}\|) & \phi(\|x_{n}-x_{2}\|) & \cdots & \phi(\|x_{n}-x_{n}\|)
\end{bmatrix}
\begin{bmatrix}
\gamma_{1} \\
\gamma_{2} \\
\vdots \\
\gamma_{n}
\end{bmatrix} = \begin{bmatrix}
g(x_{1}) \\
g(x_{2}) \\
\vdots \\
g(x_{n})
\end{bmatrix},$$
(15)

where A is the interpolation matrix. The obtained RBF interpolant s(x) can then be used to approximate the given function function g(x). Motivated by recent studies (see, e.g., [28-30, 32]), we use polyharmonic splines (PHS),

$$\phi(r) = r^m,\tag{16}$$

as the basis functions, where m is an odd positive integer.

A. RBF-FD method and augmentation with polynomials

The RBF-FD method computes a direct way to obtain the discrete representation of any linear differentiation operator \mathcal{L} at a given location x_0 as a linear combination of the function values, $g(x_i)$, such that

$$\mathcal{L}g(\mathbf{x}_0) = \sum_{j=1}^n w_j g(\mathbf{x}_j). \tag{17}$$

Here, w_j are the unknown weights and the corresponding weight vector $\mathbf{w} = [w_1, \dots, w_n]^T$ can be obtained by solving the linear system

$$\begin{bmatrix} A \end{bmatrix} \begin{bmatrix} w_1 \\ w_2 \\ \vdots \\ w_n \end{bmatrix} = \begin{bmatrix} \mathcal{L}\phi(\|x - x_1\|)\big|_{x = x_0} \\ \mathcal{L}\phi(\|x - x_2\|)\big|_{x = x_0} \\ \vdots \\ \mathcal{L}\phi(\|x - x_n\|)\big|_{x = x_0} \end{bmatrix}.$$
 (18)

An implicit assumption is that the derivative of the basis functions, $\mathcal{L}\phi$, is continuous.

Polynomial augmentation is commonly applied to the RBF-FD method to enforce consistency with Taylor expansion-based FD approximations [27, 28, 43-45]. The two-dimensional augmented RBF-FD method takes the form

$$\mathcal{L}g(\mathbf{x}_0) = \sum_{i=1}^n w_j g(\mathbf{x}_j) + \sum_{i=1}^{(q+1)(q+2)/2} c_i P_i(\mathbf{x}_0), \tag{19}$$

where $P_i(x)$ are multivariate polynomials up to degree q. To match with the local Taylor series, additional constraints for the differentiation weights,

$$\sum_{i=1}^{n} w_j P_i(\mathbf{x}_j) = \mathcal{L} P_i(\mathbf{x}_0) \qquad \text{for } 1 \le i \le \frac{(q+1)(q+2)}{2}, \tag{20}$$

are included in the computation. The use of the above constraints, also known as the vanishing momentum conditions 46, ensures that the RBF approximations locally replicate polynomial behaviour up to degree q q and decay as $r \to \infty$ q. The resulting linear system, for example of q = 1, is

$$\begin{bmatrix} A & \begin{vmatrix} 1 & x_1 & y_1 \\ \vdots & \vdots & \vdots \\ 1 & x_n & y_n \\ 1 & \cdots & 1 \\ x_1 & \cdots & x_n \\ y_1 & \cdots & y_n \end{vmatrix} \begin{bmatrix} w_1 \\ \vdots \\ w_n \\ c_1 \\ c_2 \\ c_3 \end{bmatrix} = \begin{bmatrix} \mathcal{L}\phi(||\mathbf{x} - \mathbf{x}_1||)|_{\mathbf{x} = \mathbf{x}_0} \\ \vdots \\ \mathcal{L}\phi(||\mathbf{x} - \mathbf{x}_n||)|_{\mathbf{x} = \mathbf{x}_0} \\ \mathcal{L}\mathbf{1}|_{\mathbf{x} = \mathbf{x}_0} \\ \mathcal{L}\mathbf{1}|_{\mathbf{x} = \mathbf{x}_0} \\ \mathcal{L}\mathbf{1}|_{\mathbf{x} = \mathbf{x}_0} \end{bmatrix},$$

$$(21)$$

where A is the same interpolation matrix as previously defined in equation (18). A more general and compact representation of equation (21) is

$$\begin{bmatrix} A & P \\ P^T & 0 \end{bmatrix} \begin{bmatrix} w \\ c \end{bmatrix} = \begin{bmatrix} \mathcal{L}\phi \\ \mathcal{L}P \end{bmatrix}. \tag{22}$$

Only the weight vector w is used in equation (17) to approximate the differentiation operator \mathcal{L} .

The accuracy of PHS+poly RBF-FD method depends on the stencil size, n, the PHS exponent, m, and the polynomial degree, q. In this work, we use the combination (n, m, q) = (36, 3, 3) to balance computational efficiency and physical accuracy, and achieve stability. Figure 1 shows two examples of the RBF stencil used for the spatial discretizations. The practical implementation follows 28.

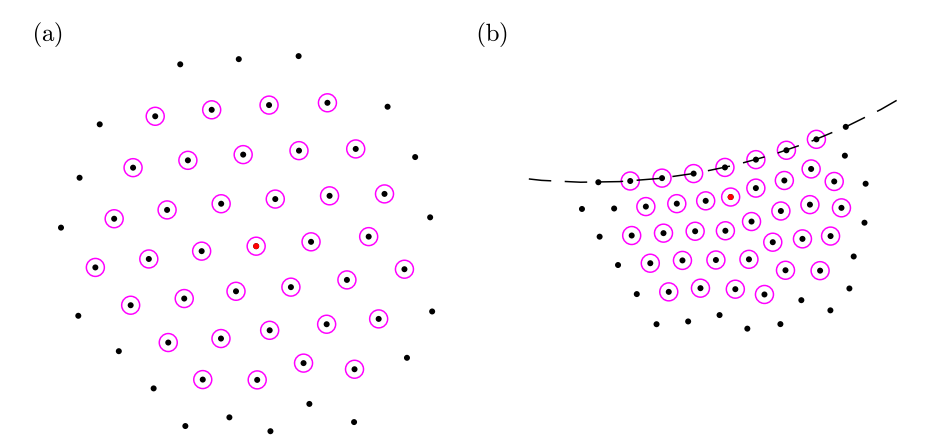


Fig. 1 RBF stencils (magenta circles) for a given node (red): (a) interior node; (b) node near domain boundary (dashed line). A constant stencil size n = 36 is used consistently.

V. Mesh-free hydrodynamic stability analysis

Differentiation matrices provides a straightforward and flexible way to discretize global Jacobians. In this work, the PHS+poly RBF-FDs are used to construct these global Jacobians on a set of scattered nodes, $\{x_i\}_{i=1}^N$. For differentiation operators $\mathcal{L} = \frac{\partial}{\partial x_k}$ and ∇^2 , we seek differentiation matrices D_{x_k} and D_{∇^2} that satisfy

$$\begin{bmatrix}
w_{11} & w_{12} & \cdots & w_{1N} \\
w_{21} & w_{22} & \cdots & w_{2N} \\
\vdots & \vdots & & \vdots \\
w_{N1} & w_{N2} & \cdots & w_{NN}
\end{bmatrix}
\begin{bmatrix}
g(\mathbf{x}_1) \\
g(\mathbf{x}_2) \\
\vdots \\
g(\mathbf{x}_N)
\end{bmatrix} = \begin{bmatrix}
\frac{\partial}{\partial x_k} g(\mathbf{x}_1) \\
\frac{\partial}{\partial x_k} g(\mathbf{x}_2) \\
\vdots \\
\frac{\partial}{\partial x_k} g(\mathbf{x}_N)
\end{bmatrix}, \quad k = 1, 2$$
(23a)

and
$$\underbrace{\begin{bmatrix} w_{11} & w_{12} & \cdots & w_{1N} \\ w_{21} & w_{22} & \cdots & w_{2N} \\ \vdots & \vdots & & \vdots \\ w_{N1} & w_{N2} & \cdots & w_{NN} \end{bmatrix}}_{\left[\begin{array}{c} g(\boldsymbol{x}_1) \\ g(\boldsymbol{x}_2) \\ \vdots \\ g(\boldsymbol{x}_N) \end{array} \right]} = \begin{bmatrix} \nabla^2 g(\boldsymbol{x}_1) \\ \nabla^2 g(\boldsymbol{x}_2) \\ \vdots \\ \nabla^2 g(\boldsymbol{x}_N) \end{bmatrix}, \tag{23b}$$

where $[x_1, x_2] = [x, y]$. The *j*th row of the sparse matrix **D** contains the $n \ll N$ weights that approximates the derivative at node x_j . The matrices hence have $N \times n$ nonzero elements.

In a slight change of notation, to enhance readability, we now denote by u = u(x) and v = v(x) the global velocity fields, and by p = p(x) the global pressure field in the computational domain Ω .

Using these differentiation matrices, we assemble the discrete global LNS operator from equation (7) as

$$L_{\overline{u}} = \begin{pmatrix} -\overline{u} \circ D_{x} - \overline{v} \circ D_{y} - \operatorname{diag}(D_{x}\overline{u}) + \operatorname{Re}^{-1}D_{\nabla^{2}} & -\operatorname{diag}(D_{y}\overline{u}) & -D_{x} \\ -\operatorname{diag}(D_{x}\overline{v}) & -\overline{u} \circ D_{x} - \overline{v} \circ D_{y} - \operatorname{diag}(D_{y}\overline{v}) + \operatorname{Re}^{-1}D_{\nabla^{2}} & -D_{y} \\ D_{x} & D_{y} & 0 \end{pmatrix}, (24)$$

where o denotes the Hadamard product. The discrete version of the linear stability eigenvalue problem, equation (6), then becomes

$$\lambda P P^T \tilde{q} = L_{\overline{u}} \tilde{q}, \tag{25}$$

where P is the prolongation matrix. The eigenvectors, $\tilde{q} = [\tilde{u}, \tilde{v}, \tilde{p}]^T$, of this generalized eigenvalue problem are referred to as the global modes.

Using the same approach, the discrete version of the input-output system, equation (13), is obtained as

$$\hat{\boldsymbol{u}} = \boldsymbol{R}(\omega)\hat{\boldsymbol{f}},\tag{26}$$

where

$$\mathbf{R}(\omega) = \mathbf{P}^T \left(i\omega \mathbf{P} \mathbf{P}^T - \mathbf{L}_{\overline{u}} \right)^{-1} \mathbf{P}$$
 (27)

is the discrete resolvent operator. The optimal input forcings, \hat{f}_j , are determined as the solutions of the generalized eigenvalue problem

$$\boldsymbol{H}(\omega)\hat{\boldsymbol{f}}_{j} = \sigma_{j}^{2} \boldsymbol{W}_{f} \hat{\boldsymbol{f}}_{j}, \tag{28}$$

where the matrix $H(\omega) = R(\omega)^* W_u R(\omega)$ is Hermitian. The optimal responses, \hat{u}_j , can then be obtained from the input-output relation

$$\hat{\boldsymbol{u}}_j = \sigma_j^{-1} \boldsymbol{R}(\omega) \hat{\boldsymbol{f}}_j. \tag{29}$$

In practice, the matrix inversion of $(i\omega PP^T - L_{\overline{u}})$ is solved using LU factorization.

VI. Application to cylinder flow

The mesh-free RBF-based hydrodynamic stability framework outlined in \P V is applied to cylinder flow at diameter-based Reynolds numbers, Re = $\frac{U_{\infty}D}{\nu}$, ranging from 47 to 180 to investigate the mean-flow stability within the two-dimensional laminar vortex shedding regime, Re \lesssim 188. The flow configuration and the mean-flow are described in the first subsection. Results of the mesh-free hydrodynamic stability analysis are presented in the second subsection.

A. Flow configuration

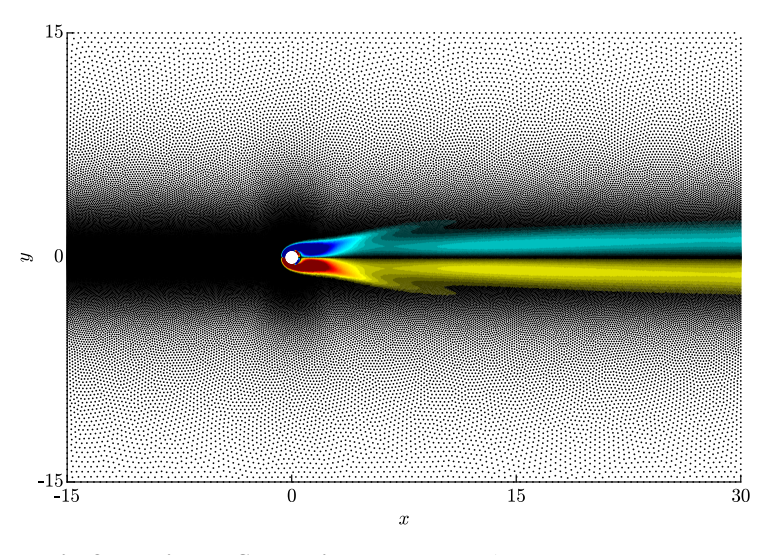


Fig. 2 Computational grid for cylinder flows with $N=118225\approx 421\times 281$ nodes, colored using the mean vorticity, $\omega=D_x\overline{\nu}-D_y\overline{u}$, at Re = 100.

We define the the computational domain Ω as the exterior of the cylinder $r \ge D/2 = 0.5$ and within the rectangle $-15 \le x \le 30$, $-15 \le y \le 15$. The computational domain is discretized by $N = 118225 \approx 421 \times 281$ scattered nodes using the unstructured triangular mesh generator DistMesh developed by [48]. We apply local grid refinement near the cylinder and around the wake centerline. The resulting node distribution is shown in Figure [2]. The characteristic distances of the grid are $\Delta r = 0.03$ near the cylinder surface, 0.04 on the wake centerline, and average at 0.087 over the whole domain. The upstream region of the cylinder has also been refined to resolve the input forcing, \hat{f} . A new

PHS+poly RBF-FD version of the fractional-step, staggered-grid algorithm by Chu and Schmdit [49] is used to simulate the unsteady cylinder flow. The mean-flow profiles, \overline{u} and \overline{v} , are obtained as the time-average of flow over 20 vortex shedding cycles. As an example, the mean vorticity at Re = 100 is showed in figure [2].

Zero-fluctuation conditions, u' = v' = 0, are prescribed on the inlet, the transverse boundaries, and on the cylinder surface. A stress-free outflow condition, $-p'n + \frac{1}{Re}\nabla u' \cdot n = 0$, where $n = [1,0]^T$ is the outflow direction, is enforced at the outflow. For the resolvent analysis, the inner products defined in equation (11) are calculated with an identity weight matrix, $W_u = W_f = I$, to account for the integral perturbation kinetic energy within the computational domain.

B. Results

1. Mean-flow stability analysis

As a validation case for the new code, we choose the now classical mean-flow stability analyses of the cylinder wake by Pier [5] and Barkley [6].

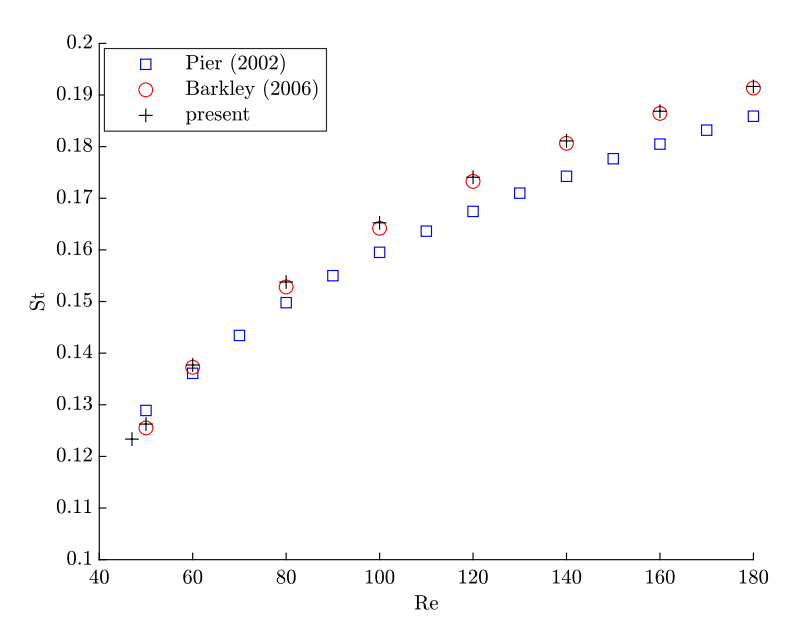


Fig. 3 Vortex shedding frequency predicted by the leading eigenvalue of the mean-flow stability problem as a function of Reynolds number. The frequency is given as the non-dimensional Strouhal number $St = \lambda_i/2\pi$. Shown for comparison are results from Pier [5] (blue square) and Barkley [6] (red circle).

Figure 3 shows the frequencies associated with the leading eigenvalues from the linear analysis of the mean-flow. The nondimensional cylinder wake eigenfrequencies are expressed in terms of the Strouhal number, $St = \lambda_i/2\pi$. Starting from the critical Reynolds number of $Re_c \approx 47$ the frequency-Reynolds number dependence exhibits the typical characteristics of a Hopf bifurcation. Our results compare well to Barkley 6, and just like Barkley 6, deviate no more than 3% from those by Pier 5. The corresponding growth rates are almost identical to zero (see also figures 4 and 6 below), confirming that the mean-flow is marginally stable. Next, we conduct a comparative study of linear stability and resolvent analysis, both in terms of spectra and modes, at two representative Reynolds numbers, $Re_c \approx 47$ and Re = 100.

2. Comparative study of linear stability and resolvent analysis at $Re_c \approx 47$ and Re = 100

Before studying the modes in more detail, we first examine the resolvent singular value and stability eigenvalue spectra to confirm that peaks in the resolvent gain are associated with an eigenvalue. Figure $\frac{1}{4}$ shows the spectra for the critical Reynolds number of Re = 47. Both the peak of the resolvent gain and the leading eigenvalue identify the same frequency, St = 0.1199, as the vortex shedding frequency. Next, will confirm that the associated modes describe the vortex shedding flow structure.

Figure 5 shows the leading stability and resolvent modes for the cylinder mean-flow at Re = 47. A comparison of

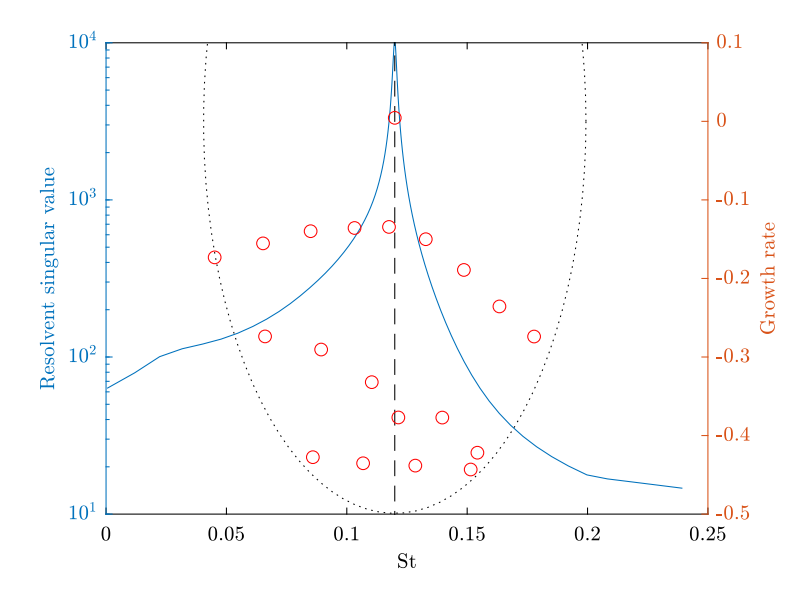


Fig. 4 Resolvent singular values (blue curve) and stability eigenvalue (red circle) spectra for Re = 47. The 20 eigenvalues closest to $\lambda = 0 + 0.753i$ were found within the region outlined by the black dotted line using the shift-and-invert Arnoldi algorithm.

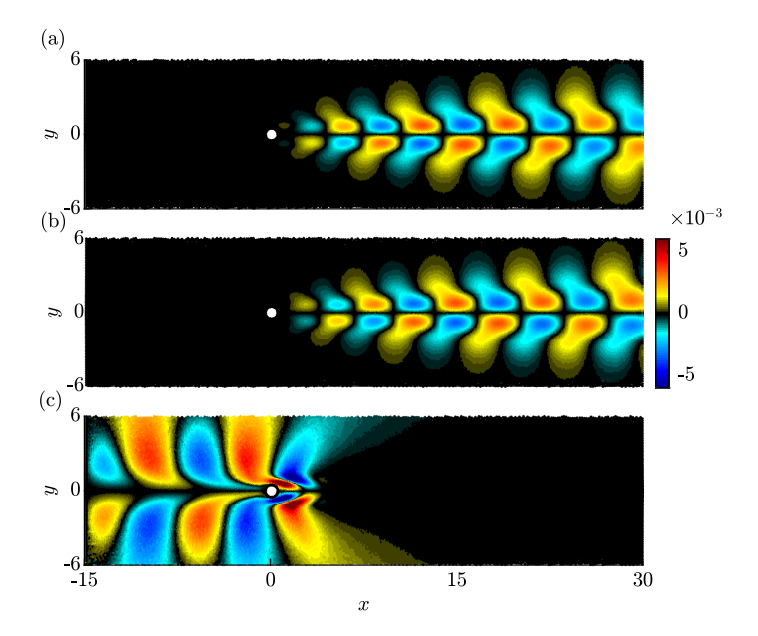


Fig. 5 Leading modes for Re = 47 at St = 0.1199: (a) stability mode; (b) response mode; (c) forcing mode.

subplots [5(a) and [5(b) shows that the leading stability and response modes are near-identical up to a shift in phase, which is undetermined in both analyses, and correspond to the typical vortex shedding structure. The similarity between the stability and resolvent response modes is not unexpected as the singular value of the resolvent peaks at the vortex shedding frequency [19] [39]. In other words, the optimal forcing leverages the globally instability mode to attain maximum gain. In contrast to the optimal response and global modes, the optimal forcing mode extends upstream, but peaks downstream in close vicinity to the cylinder. This is the hallmark of convective instability. Similar flow patterns were observed in previous work by [39] [50] [51].

Next, we repeat the same analysis for the unsteady regime at Re = 100. Figure 6 shows the corresponding resolvent singular value and stability eigenvalue spectra. Similar to what was found for figure 4, the resolvent singular value

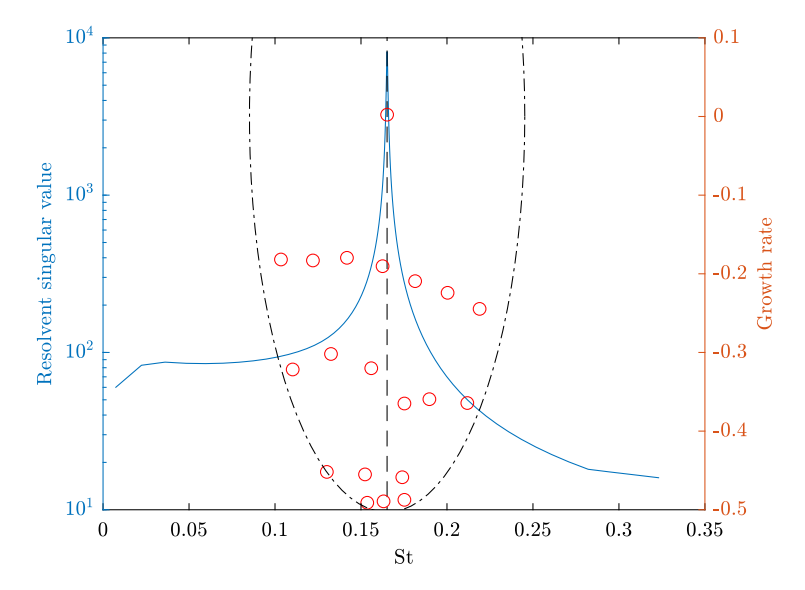


Fig. 6 Same as figure $\frac{4}{9}$ for Re = 100 with vortex shedding frequency St = 0.1652.

spectrum displays a clear peak at the vortex shedding frequency, which is now St = 0.1652, and again coinciding with the least stable global eigenvalue.

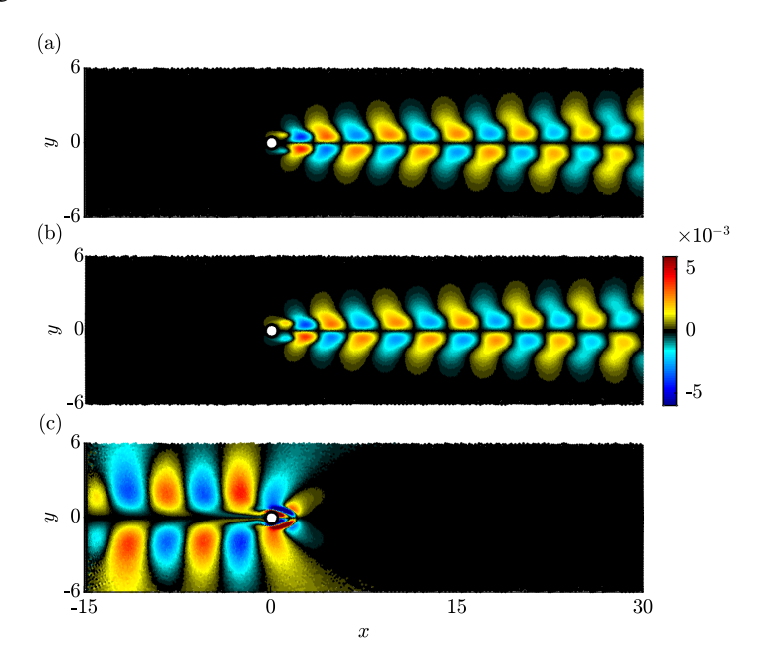


Fig. 7 Same as figure $\frac{5}{5}$ for Re = 100 with vortex shedding frequency St = 0.1652.

Figure 7 shows the leading stability and resolvent modes for the cylinder mean-flow at Re = 100. Similar to what was observed in figure 5 the leading stability and response modes represent the same flow structure associated with the vortex shedding.

VII. Summary

We have developed a higher-order mesh-free framework for hydrodynamic stability analysis based on a PHS+poly RBF-FD discretization. The PHS-type RBFs with polynomial augmentation were shown to yield accurate, stable, and

computationally efficient discretizations of large hydrodynamic stability matrix problems on scattered nodes. The obtained differentiation matrices are used to form the discrete linearized Navier-Stokes operator for both the stability and resolvent analysis. Vortex shedding behind a 2D cylinder is studied as an example to demonstrate the framework. Flow instabilities, including the vortex shedding frequency and associated coherent structures, are accurately predicted.

Acknowledgments

The authors would like to thank Bengt Fornberg for sharing his insights. We gratefully acknowledge support by the National Science Foundation under Grant No. CBET-1953999 (PM Ron Joslin).

References

- [1] Mattingly, G. E., and Criminale, W. O., "The stability of an incompressible two-dimensional wake," *J. Fluid Mech.*, Vol. 51, No. 2, 1972, pp. 233–272.
- [2] Noack, B. R., and Eckelmann, H., "A global stability analysis of the steady and periodic cylinder wake," *J. Fluid Mech.*, Vol. 270, 1994, pp. 297–330.
- [3] Monkewitz, P. A., Huerre, P., and Chomaz, J.-M., "Global linear stability analysis of weakly non-parallel shear flows," *J. Fluid Mech.*, Vol. 251, 1993, pp. 1–20.
- [4] Woodley, B. M., and Peake, N., "Global linear stability analysis of thin aerofoil wakes," *J. Fluid Mech.*, Vol. 339, 1997, pp. 239–260.
- [5] Pier, B., "On the frequency selection of finite-amplitude vortex shedding in the cylinder wake," J. Fluid Mech., Vol. 458, 2002, pp. 407–417.
- [6] Barkley, D., "Linear analysis of the cylinder wake mean flow," Europhys. Lett., Vol. 75, No. 5, 2006, p. 750.
- [7] Sipp, D., and Lebedev, A., "Global stability of base and mean flows: a general approach and its applications to cylinder and open cavity flows," *J. Fluid Mech.*, Vol. 593, 2007, pp. 333–358.
- [8] Gudmundsson, K., and Colonius, T., "Instability wave models for the near-field fluctuations of turbulent jets," *J. Fluid Mech.*, Vol. 689, 2011, pp. 97–128.
- [9] Oberleithner, K., Rukes, L., and Soria, J., "Mean flow stability analysis of oscillating jet experiments," *J. Fluid Mech.*, Vol. 757, 2014, pp. 1–32.
- [10] Jovanović, M. R., and Bamieh, B., "Componentwise energy amplification in channel flows," J. Fluid Mech., Vol. 534, 2005, pp. 145–183.
- [11] Moarref, R., and Jovanović, M. R., "Model-based design of transverse wall oscillations for turbulent drag reduction," *J. Fluid Mech.*, Vol. 707, 2012, pp. 205–240.
- [12] Monokrousos, A., Åkervik, E., Brandt, L., and Henningson, D. S., "Global three-dimensional optimal disturbances in the Blasius boundary-layer flow using time-steppers," *J. Fluid Mech.*, Vol. 650, 2010, pp. 181–214.
- [13] Sipp, D., and Marquet, O., "Characterization of noise amplifiers with global singular modes: the case of the leading-edge flat-plate boundary layer," *Theor. Comput. Fluid Dyn.*, Vol. 27, No. 5, 2013, pp. 617–635.
- [14] Garnaud, X., Lesshafft, L., Schmid, P. J., and Huerre, P., "The preferred mode of incompressible jets: linear frequency response analysis," *J. Fluid Mech.*, Vol. 716, 2013, pp. 189–202.
- [15] Jeun, J., Nichols, J. W., and Jovanović, M. R., "Input-output analysis of high-speed axisymmetric isothermal jet noise," *Phys. Fluids*, Vol. 28, No. 4, 2016, p. 047101.
- [16] Semeraro, O., Lesshafft, L., Jaunet, V., and Jordan, P., "Modeling of coherent structures in a turbulent jet as global linear instability wavepackets: theory and experiment," *Int. J. Heat Fluid Flow.*, Vol. 62, 2016, pp. 24–32.
- [17] McKeon, B. J., and Sharma, A. S., "A critical-layer framework for turbulent pipe flow," *J. Fluid Mech.*, Vol. 658, 2010, pp. 336–382.
- [18] Sharma, A. S., and McKeon, B. J., "On coherent structure in wall turbulence," J. Fluid Mech., Vol. 728, 2013, pp. 196–238.

- [19] Beneddine, S., Sipp, D., Arnault, A., Dandois, J., and Lesshafft, L., "Conditions for validity of mean flow stability analysis," J. Fluid Mech., Vol. 798, 2016, pp. 485–504.
- [20] Jacobi, I., and McKeon, B. J., "Dynamic roughness perturbation of a turbulent boundary layer," *J. Fluid Mech.*, Vol. 688, 2011, pp. 258–296.
- [21] Bae, H. J., Dawson, S. T. M., and McKeon, B. J., "Resolvent-based study of compressibility effects on supersonic turbulent boundary layers," J. Fluid Mech., Vol. 883, 2020.
- [22] Towne, A., Schmidt, O. T., and Colonius, T., "Spectral proper orthogonal decomposition and its relationship to dynamic mode decomposition and resolvent analysis," J. Fluid Mech., Vol. 847, 2018, pp. 821–867.
- [23] Schmidt, O. T., Towne, A., Rigas, G., Colonius, T., and Brès, G. A., "Spectral analysis of jet turbulence," *J. Fluid Mech.*, Vol. 855, 2018, pp. 953–982.
- [24] Yeh, C.-A., and Taira, K., "Resolvent-analysis-based design of airfoil separation control," J. Fluid Mech., Vol. 867, 2019, pp. 572–610.
- [25] Hardy, R. L., "Multiquadric equations of topography and other irregular surfaces," J. Geophys. Res., Vol. 76, No. 8, 1971, pp. 1905–1915.
- [26] Tolstykh, A. I., "On using RBF-based differencing formulas for unstructured and mixed structured-unstructured grid calculations," Proceedings of the 16th IMACS world congress, Vol. 228, Lausanne, 2000, pp. 4606–4624.
- [27] Fornberg, B., and Flyer, N., "Solving PDEs with radial basis functions," Acta Numer., Vol. 24, 2015, p. 215.
- [28] Flyer, N., Barnett, G. A., and Wicker, L. J., "Enhancing finite differences with radial basis functions: experiments on the Navier–Stokes equations," *J. Comput. Phys.*, Vol. 316, 2016, pp. 39–62.
- [29] Flyer, N., Fornberg, B., Bayona, V., and Barnett, G. A., "On the role of polynomials in RBF-FD approximations: I. Interpolation and accuracy," J. Comput. Phys., Vol. 321, 2016, pp. 21–38.
- [30] Bayona, V., Flyer, N., Fornberg, B., and Barnett, G. A., "On the role of polynomials in RBF-FD approximations: II. Numerical solution of elliptic PDEs," *J. Comput. Phys.*, Vol. 332, 2017, pp. 257–273.
- [31] Bayona, V., "An insight into RBF-FD approximations augmented with polynomials," Comput. Math. with Appl., Vol. 77, No. 9, 2019, pp. 2337–2353.
- [32] Bayona, V., Flyer, N., and Fornberg, B., "On the role of polynomials in RBF-FD approximations: III. Behavior near domain boundaries," *J. Comput. Phys.*, Vol. 380, 2019, pp. 378–399.
- [33] Santos, L. G. C., Manzanares-Filho, N., Menon, G. J., and Abreu, E., "Comparing RBF-FD approximations based on stabilized Gaussians and on polyharmonic splines with polynomials," *Int. J. Numer. Methods Eng.*, Vol. 115, No. 4, 2018, pp. 462–500.
- [34] Bayona, V., "Comparison of moving least squares and RBF+ poly for interpolation and derivative approximation," *J. Sci. Comput.*, Vol. 81, No. 1, 2019, pp. 486–512.
- [35] Bénard, H., "The formation of gyration centres at the back of a moving obstacle," C. R. Acad. Sci., Vol. 147, 1908, pp. 839-842.
- [36] Vón Kármán, T., "Über den Mechanismus des Widerstandes, den ein bewegter Körper in einer Flüssigkeit erfährt," *Göttingen Nachr. Math. Phys. Kl.*, Vol. 1911, 1911, pp. 509–517.
- [37] Provansal, M., Mathis, C., and Boyer, L., "Bénard-von Kármán instability: transient and forced regimes," *J. Fluid Mech.*, Vol. 182, 1987, pp. 1–22.
- [38] Sreenivasan, K. R., Strykowski, P. J., and Olinger, D. J., "Hopf bifurcation, Landau equation, and vortex shedding behind circular cylinders," *Forum on unsteady flow separation*, Vol. 1, ASME New York, 1987, pp. 1–13.
- [39] Symon, S., Rosenberg, K., Dawson, S. T. M., and McKeon, B. J., "Non-normality and classification of amplification mechanisms in stability and resolvent analysis," *Phys. Rev. Fluids*, Vol. 3, No. 5, 2018, p. 053902.
- [40] Barkley, D., and Henderson, R. D., "Three-dimensional Floquet stability analysis of the wake of a circular cylinder," J. Fluid Mech., Vol. 322, 1996, pp. 215–241.
- [41] Williamson, C., "Vortex dynamics in the cylinder wake," Annu. Rev. Fluid Mech., Vol. 28, No. 1, 1996, pp. 477–539.

- [42] Schmid, P., and Henningson, D., Stability and Transition in Shear Flows, Applied Mathematical Sciences, Springer New York, 2000.
- [43] Fornberg, B., and Lehto, E., "Stabilization of RBF-generated finite difference methods for convective PDEs," *J. Comput. Phys.*, Vol. 230, No. 6, 2011, pp. 2270–2285.
- [44] Larsson, E., Lehto, E., Heryudono, A., and Fornberg, B., "Stable computation of differentiation matrices and scattered node stencils based on Gaussian radial basis functions," *SIAM J. Sci. Comput.*, Vol. 35, No. 4, 2013, pp. A2096–A2119.
- [45] Wright, G. B., and Fornberg, B., "Scattered node compact finite difference-type formulas generated from radial basis functions," *J. Comput. Phys.*, Vol. 212, No. 1, 2006, pp. 99–123.
- [46] Iske, A., "On the approximation order and numerical stability of local Lagrange interpolation by polyharmonic splines," *Modern developments in multivariate approximation*, Springer, 2003, pp. 153–165.
- [47] Fornberg, B., Driscoll, T. A., Wright, G., and Charles, R., "Observations on the behavior of radial basis function approximations near boundaries," *Comput. Math. with Appl.*, Vol. 43, No. 3-5, 2002, pp. 473–490.
- [48] Persson, P.-O., "Mesh generation for implicit geometries," Ph.D. thesis, Massachusetts Institute of Technology, 2005.
- [49] Chu, T., and Schmdit, O. T., "An RBF-based finite difference discretization of the Navier-Stokes equations: error analysis and application to lid-driven cavity flow," *AIAA AVIATION 2021 FORUM*, 2021, p. 2743.
- [50] Marquet, O., Sipp, D., and Jacquin, L., "Sensitivity analysis and passive control of cylinder flow," J. Fluid Mech., Vol. 615, 2008, pp. 221–252.
- [51] Jin, B., Symon, S., and Illingworth, S. J., "Energy transfer mechanisms and resolvent analysis in the cylinder wake," *Physical Review Fluids*, Vol. 6, No. 2, 2021, p. 024702.